Original Article

The lysosomal protein arylsulfatase B is a key enzyme involved in skeletal turnover†

Running Title: Arsb is required for bone remodeling

Sandra Pohl[1,*], Alexandra Angermann[2,*], Anke Jeschke[2,*], Gretl Hendrickx[2], Timur A Yorgan[2], Georgia Makrypidi-Fraune[1], Anita Steigert[2], Sonja C Kuehn[2], Tim Rolvien[2], Michaela Schweizer[3], Till Koehne[2,4], Mona Neven[2], Olga Winter[2], Renata Voltolini Velho[1], Joachim Albers[2], Thomas Streichert[5], Jan M Pestka[2], Christina Baldauf[2], Sandra Breyer[6], Ralf Stuecker[6], Nicole Muschol[3], Timothy M Cox[7], Paul Saftig[8], Chiara Paganini[9], Antonio Rossi[9], Michael Amling[2], Thomas Braulke[1], and Thorsten Schinke[2]

[1]Department of Biochemistry, Children´s Hospital, University Medical Center Hamburg-Eppendorf, Hamburg 20246, Germany.

[2]Department of Osteology and Biomechanics, University Medical Center Hamburg-Eppendorf, Hamburg 20246, Germany.

[3]Department of Electron Microscopy, Center of Molecular Neurobiology, University Medical Center Hamburg-Eppendorf, Hamburg 20246, Germany.

[4]Department of Orthodontics, University Medical Center Hamburg-Eppendorf, Hamburg 20246, Germany.

[5]Department of Clinical Chemistry, University Hospital Cologne, Cologne 50937, Germany.

[6]Department of Orthopedics, Children´s Hospital Hamburg-Altona, Hamburg 22763, Germany.

[7]Department of Medicine, University of Cambridge, Cambridge, CB21TN, UK.

[8]Institute of Biochemistry, Christian-Albrechts-University, Kiel 24098, Germany.

[9]Department of Molecular Medicine, University of Pavia, Pavia 27100, Italy.

[*]These authors contributed equally to this work.

Address correspondence to: Thorsten Schinke, PhD, Department of Osteology and Biomechanics, University Medical Center Hamburg Eppendorf, Martinistrasse 52, Hamburg 20246, Germany. Phone: +49-40-7410-58057. E-mail: schinke@uke.de

†This article has been accepted for publication and undergone full peer review but has not been through the copyediting, typesetting, pagination and proofreading process, which may lead to differences between this version and the Version of Record. Please cite this article as doi: [10.1002/jbmr.3563]

Additional Supporting Information may be found in the online version of this article.

Initial Date Submitted March 12, 2018; Date Revision Submitted July 10, 2018; Date Final Disposition Set July 20, 2018

Journal of Bone and Mineral Research

DOI 10.1002/jbmr.3563

Grant supporters: The research leading to these results has received funding from the European Community's Seventh Framework Programme under grant agreement n°602300 (SYBIL), from the European Union's Horizon 2020 research and innovation program under the Marie Sklodowska-Curie grant agreement No 794386, and from grants by the Deutsche Forschungsgemeinschaft (AM 103/25-1, SCHI 504/8-1, PO 1539/1-1, SFB877).

This submission includes supplemental material.

Disclosure Page

All authors state that they have no conflict of interest.

ABSTRACT

Skeletal pathologies are frequently observed in lysosomal storage disorders, yet the relevance of specific lysosomal enzymes in bone remodeling cell types is poorly defined. Two lysosomal enzymes, i.e. Ctsk (cathepsin K) and Acp5 (also known as tartrate-resistant acid phosphatase), are long known as molecular marker proteins of differentiated osteoclasts. However, whereas the cysteine protease Ctsk is directly involved in the degradation of bone matrix proteins, the molecular function of Acp5 in osteoclasts is still unknown. Here we show that Acp5, in concert with Acp2 (lysosomal acid phosphatase), is required for dephosphorylation of the lysosomal mannose 6-phosphate targeting signal to promote the activity of specific lysosomal enzymes. Using an unbiased approach we identified the glycosaminoglycan-degrading enzyme Arsb (arylsulfatase B), mutated in mucopolysaccharidosis type VI (MPS-VI), as an osteoclast marker, whose activity depends on dephosphorylation by Acp2 and Acp5. Similar to *Acp2/Acp5*$^{-/-}$ mice, Arsb-deficient mice display lysosomal storage accumulation in osteoclasts, impaired osteoclast activity and high trabecular bone mass. Of note, the most prominent lysosomal storage was observed in osteocytes from *Arsb*-deficient mice, yet this pathology did not impair production of Sost and Fgf23. Since the influence of enzyme replacement therapy (ERT) on bone remodeling in MPS-VI is still unknown, we additionally treated *Arsb*-deficient mice by weekly injection of recombinant human ARSB from 12 to 24 weeks of age. We found that the high bone mass phenotype of Arsb-deficient mice and the underlying bone cell deficits were fully corrected by ERT in the trabecular compartment. Taken together, our results do not only demonstrate that the function of Acp5 in osteoclasts is linked to dephosphorylation and activation of lysosomal enzymes, they also provide an important proof-of-principle for the feasibility of ERT to correct bone cell pathologies in lysosomal storage disorders.

Keywords: arylsulfatase B, lysosomal storage disorders, mucopolysaccharidosis type VI, tartrate-resistant acid phosphatase

Introduction

Osteoclasts are highly specialized multinucleated cells, which are generated by fusion of hematopoietic progenitors in a process initiated by two major cytokines, i.e. M-Csf and Rankl (1, 2). It was previously reported that Rankl activates Tfeb (transcription factor EB), a transcription factor inducing lysosomal gene expression, and that Tfeb inactivation in osteoclasts impairs their resorptive activity to trigger a high bone mass phenotype (3). The relevance of lysosome biogenesis for osteoclast function is supported by the fact that two specific lysosomal enzymes, Ctsk and Acp5, serve as molecular markers of differentiated osteoclasts (4, 5). However, while Ctsk is directly involved in the degradation of bone matrix proteins, the molecular mechanism of Acp5 action in osteoclasts remains to be clarified. The participation of Acp5 in physiological bone resorption is supported by genetic evidence in mice and humans. More specifically, *Acp5*$^{-/-}$ mice are growth-retarded due to impaired endochondral ossification and thickening of subchondral bone (6). They were also found to display reduced clearance of bacteria and functionally impaired dendritic cells (7, 8). Mutations in human *ACP5* were reported to cause spondyloenchondrodysplasia, a rare disorder associated with bone dysplasia and autoimmunity (9, 10). However, the skeletal manifestations in these patients are less severe than in other forms of osteopetrosis, and the osteopetrotic phenotype of *Acp5*$^{-/-}$ mice is rather moderate compared to other models, such as mice lacking M-Csf, Rankl, Clc-7 or Tcirg1 (11-14). One possible explanation is a functional redundancy between Acp5 and Acp2, since we have previously observed that mice lacking both genes display more severe osteopetrosis and hepatosplenomegaly (15).

Lysosomes are required for degradation and recycling of numerous macromolecules (16). The inherited deficiency of single lysosomal enzymes causes lysosomal storage disorders, which are often associated with various defects of skeletal development and growth, summarized as dysostosis multiplex (17, 18). Mucopolysaccharidoses (MPS) represent a subgroup of lysosomal storage disorders, which are caused by the single loss of eleven different

enzymes involved in the breakdown of glycosaminoglycans (GAGs). This results in lysosomal accumulation of non-degradable intermediate forms of specific GAGs, i.e. chondroitin sulfate (CS), dermatan sulfate (DS), heparan sulfate (HS), or keratan sulfate (KS) (19). Depending on the mutated enzyme and the type of accumulating GAGs distinct organs are specifically affected in the different MPS types. For instance, mutations in the *IDUA* gene (coding for α-L-iduronidase required for DS and HS degradation) cause severe neurological and skeletal manifestation in individuals with MPS-I, whereas mutations in the *SGSH* gene (coding for sulfamidase required for HS and KS degradation) cause neurological deficits in MPS-IIIA patients, without profoundly affecting the skeleton (20, 21). In contrast, MPS-VI, caused by mutations of the *ARSB* gene (coding for arylsulfatase B involved in CS and DS degradation) is primarily associated with skeletal defects, but lacks neurological manifestation (22).

One of the leading treatment options for some forms of MPS is enzyme replacement therapy (ERT), i.e. weekly (or biweekly) infusion of the missing recombinant enzyme modified with mannose 6-phosphate (M6P) residues to allow M6P receptor-mediated cellular uptake and lysosomal delivery (23, 24). ERT has been proven to attenuate disease progression in the respective individuals, yet it appeared to have limited therapeutic efficacy on the skeletal abnormalities, since existing defects of skeletal growth and craniofacial bones were not obviously corrected (25). Moreover, although effects of ERT on potential disturbances of bone remodeling in individuals with MPS have not been analyzed so far, it was generally assumed that the responsible skeletal cell types are poorly accessible to the circulating recombinant enzymes (26).

Here we show that Acp5, in concert with Acp2, promotes osteoclast activity by M6P dephosphorylation of Arsb and other lysosomal enzymes. Both, *Acp2/Acp5*$^{-/-}$ and Arsb-deficient mice, display lysosomal storage accumulation in osteoclasts, impaired osteoclast activity and high trabecular bone mass. Importantly, the trabecular bone phenotype of Arsb-deficient mice was fully corrected by ERT, which was molecularly explained by the ability of osteoclasts to

endocytose recombinant ARSB in an M6P receptor-independent manner. Our results reveal that Arsb is a physiologically relevant substrate of Acp2/Acp5, which is required for skeletal turnover and which can be administered systemically to correct trabecular bone pathologies.

Materials and Methods

Animals

Mice lacking *Acp2* or *Acp5* have been described previously (15). Genotyping for the *Acp2* mutation was performed by PCR (5´-CCC CTC TGC CTC ACC TCT CTG-3´ and 5´-GGC AAC TAG CAG GGA TGG CCG-3´) amplifying a genomic fragment of 400 bp (wildtype allele) or 1500 bp (mutant allele). Genotyping for the *Acp5* mutation was performed by PCR (5´-AGC GCT TTC CTG ACT GAG CTG C-3´ and 5´-AAC CGT GCA GAC GAT GGG CG-3) amplifying a genomic fragment of 1000 bp (wildtype allele) or 2000 bp (mutant allele). *Ctsk*-deficient mice (27) were obtained from the European Mutant Mouse Archive (EMMA; ID #10406). Genotyping for the *Ctsk* mutation was performed by PCR (5´- GCC ACA CCC ACA CCC TAG AAG-3´ and 5´- ACA AGT GTA CAT TCC CGT ACC-3) amplifying a genomic fragment of 350 bp (wildtype allele) or 1500 bp (mutant allele). *Arsb*$^{+/m}$ mice were obtained from the Jackson Laboratory (#005598). Offspring from heterozygous matings was genotyped by sequencing of a PCR amplicon (primers 5´-GCT ATA TCA CGG GCA CTA ATC C-3´ and 5´-TAT CGA ATC CTC GGC GTG T-3´) for the presence of mutation c.379G>T in exon 2. After initially confirming that the observed abnormalities are found to the same extent in male and female *Arsb*$^{m/m}$ mice, we focused on female mice for the remaining analysis. We also analyzed heterozygous *Arsb*$^{+/m}$ mice and found no significant alterations compared to wildtype littermates. *Hyp* mice were obtained from the Jackson Laboratory (#000528), and their genotyping was performed by genomic PCR. More specifically, while the presence of the *Phex* exon 21 was detected using 5´-CGA CCA GGA TGA GGG AAG AAA G -3´ and 5´-CAC TTG TTC TCT GGC AGC TTC TG-3´ (486 bp product), the *Hyp* mutation was detected by 5'-CAG

GGG ACT GTC CAC AAG GGG G-3' and 5'-GGG TGC AAA GGT GTT GTG AAT GGA A-3' (669 bp product). All mice were kept in a specific pathogen-free environment with a 12-hour light/dark cycle, 45% to 65% relative humidity and 20°C to 24°C ambient temperature in open or individually ventilated cages with wood shavings bedding and nesting material in groups not surpassing 6 animals. The mice had access to tap water and standard rodent chow (1328P, Altromin Spezialfutter GmbH & Co. KG, Lage, Germany) ad libitum. All animal experiments were approved by the animal facility of the University Medical Center Hamburg-Eppendorf and by the "Amt für Gesundheit und Verbraucherschutz" (43/15, Org529). To rule out any influence unrelated to genotype, we generally analyzed littermate mice from heterozygous matings. Depending on the models (single versus combined deficiency) we analyzed the corresponding mice from three to six independent litters.

Skeletal analysis

Staining of skeletons from 4 weeks old mice with alcian blue and alizarin red was performed using standard protocols (28). To determine the length of the lumbar spine and the long bones, all mice were analyzed by contact Xray. Dissected skeletons were fixed in 3.7% PBS-buffered formaldehyde for 18 hours, before they were stored in 80% ethanol. The lumbar vertebral bodies L1 to L4 and one tibia were dehydrated in ascending alcohol concentrations and then embedded in methylmetacrylate as described previously (29). Sections of 4 µm thickness were cut in the sagittal plane and stained by toluidine blue or von Kossa/van Gieson staining procedures. Histomorphometry was performed according to the ASBMR guidelines using the OsteoMeasure system (Osteometrics Inc.) (30). For µCT scanning we used a µCT 40 desktop cone-beam microCT (Scanco Medical) with a voxel size of 10 µm.

Primary bone cells

For osteoclastogenesis, bone marrow was flushed out of the femora from 12 weeks old mice with alpha-MEM (minimal essential medium) containing 10% fetal bovine serum (alpha-MEM/FBS). Cells were then plated at a density of 5 x 10^6 cells per ml, and after 24 hours the adherent cells were cultured in alpha-MEM/FBS containing 10% fetal bovine serum and 10 nM 1,25-dihydroxyvitamin-D3. Beginning at day 4 after seeding M-Csf and Rankl (both from Peprotech) were added to a final concentration of 20 ng/ml and 40 ng/ml, respectively. TRAP staining was performed at day 7 of differentiation as described using Naphtol ASMX-Phosphate (Sigma-Aldrich) as a substrate (29). For resorption assays, bone marrow cells were seeded onto dentin slices of 1 mm thickness. After 10 days of differentiation, the resorbed areas were visualized and quantified as described (29). Primary osteoblasts were isolated by sequential collagenase digestion from the calvariae of 5 days old mice and differentiated in the presence of 50 µg/ml ascorbic acid and 10 mM ß-glycerophosphate for 20 days.

Expression analysis

RNA was isolated using the RNeasyMini kit (Qiagen), and DNase digestion was performed according to manufacturer's instructions. Concentration and quality of RNA were measured using a NanoDrop ND-1000 system (NanoDrop Technology). Expression analysis by qRT-PCR was performed using a StepOnePlus system and predesigned TaqMan gene expression assays (Applied Biosystems). *Gapdh* expression was used as an internal control. Relative quantification was performed according to the $\Delta\Delta C_T$ method, and results were expressed in the linear form using the formula $2^{-\Delta\Delta CT}$. For genome-wide expression analysis we used the IVT Labeling Kit (Affymetrix). Gene Chips (Affymetrix MG 430 2.0) were washed in an Affymetrix Fluidics Station 450, and microarrays were scanned with the Affymetrix Gene Chip Scanner 7G. Annotations were analyzed with interactive query analysis at www.affymetrix.com, and data sets were submitted to GEO (GSE94691).

Enzyme activity assays

The enzymatic activities of lysosomal enzymes in protein extracts and serum-free media of cultured cells were assayed by estimation of 4-nitrophenol or 4-methylumbelliferone liberated from the enzyme-specific substrate. The activities of β-hexosaminidase, β-galactosidase, α-mannosidase, ß-glucuronidase, Arsb, Acp2 and Acp5 were determined as described previously (31-33). The Ctsk activity was assayed using 20 µM Z-Leu-Arg-7-amino-4-methylcoumarin (Enzo Life Sciences) in 100 mM Na-citrate (pH 5.0), 100 mM NaCl, 1 mM EDTA, 5 mM dithiothreitol (DTT) and 1% DMSO. The assay was stopped by addition of 0.4 M glycine/NaOH buffer (pH 10.4) after 17 hours and the fluorescence of samples and standard solutions of 7-amino-4-methylcoumarin were read with excitation at 355 nm and emission at 460 nm.

Western blot analysis

Unless otherwise described, cells were lysed in 10 mM PBS (pH 7.4) containing 0.5% Triton X-100 and protease inhibitors for 30 minutes at 4 °C. After centrifugation at 10,000 × g, supernatants were used for measurement of the protein content by the Bio-Rad® Protein Assay. Aliquots of cell extracts (25 µg protein) or recombinant ARSB (50 ng) were solubilized, separated by reducing SDS-PAGE (10% acrylamide) and transferred onto nitrocellulose membranes. Western blots were performed using antibodies against human ARSB (R&D, #MAB4415), mouse Ctsk (Santa Cruz Biotechnology, #sc-48353), mouse Clc7 (kindly provided by Dr. T. Jentsch, MDC, Berlin, Germany (13), mouse Lamp1 (clone 1D4B, Hybridoma Bank, University of Iowa, USA), mouse Limp2 (kindly provided by Dr. M. Schwake, University Bielefeld, Germany (34) or calnexin (Canx, Enzo Life Sciences, ADI-SPA-865), the latter serving as loading control, as previously described (33). The content of M6P-containing proteins in cell extracts were analyzed by western blotting using a single chain antibody fragment scFv M6P-1 as described (35).

Two-dimensional gel eletrophoresis

Primary osteoclasts were washed three times with cold PBS, harvested and lysed in 500 µl initial buffer (8 M urea, 15 mM EDTA, 30 mM Tris, 50 mM DTT) supplemented with protease inhibitor cocktail and PhosphoStop (Roche). After addition of 2-hydroxyethyl disulfide (HED) to a final concentration of 20 mM cell lysates were homogenized on ice by ultrasonic treatment using 3 steps (amplitude 100%, 20 seconds). After incubation for 60 minutes at room temperature, samples were centrifuged at 15.000 x g for 5 minutes and supernatants were collected. Total proteins were precipitated and quantified using 2-D Quant Kit (GE Healthcare). Aliquots (25 µg protein) were then subjected to two-dimensional gel electrophoresis and blotted on nitrocellulose membrane as described (36).

ARSB uptake assays

To monitor cellular uptake of ARSB, cultured osteoblasts or osteoclasts were incubated for 4 hours with serum-free Opti-MEM™ medium containing 10 µg/ml human recombinant ARSB (Naglazyme®, kindly provided by Dr. M. Vellard, BioMarin) in the presence or absence of 20 mM M6P and/or 80 mM mannose (both from Sigma-Aldrich).

Immunofluorescence microscopy

Primary cultured osteoclasts grown on cover slips were fixed with 4% paraformaldehyde in PBS for 30 minutes. After washing with 50 mM ammonium chloride, cells were permeabilized with 0.1% saponine in PBS for 10 minutes and blocked in PBS containing 0.1% saponine and 3% bovine serum albumin for 30 minutes. Subsequently, cells were incubated with primary antibodies against Lamp1 (clone 1D4B, Hybridoma Bank, University of Iowa, USA) for 2 hours. After washing with 0.1% saponine in PBS, cells were incubated with secondary antibodies conjugated to Alexa Fluor® 488 (Thermo Fisher Scientific), and 4′,6-diamidino-2-

phenylindole (DAPI) for 1 hour and embedded in Aqua-Poly/Mount. Fluorescence was detected and images were obtained using an Olympus digital scanning confocal microscope (FluoView F1000) and Adobe Photoshop software, respectively.

Electron microscopy

For ultrastructural analysis, tibiae were fixed with 4% paraformaldehyde and 1% glutaraldehyde in 0.1 M PBS (pH 7.4) overnight and decalcified for 3 to 4 weeks in 10% EDTA. Thereafter 100 µm thick vibratome sections were prepared and postfixed in 1% OsO4, dehydrated and embedded in Epon™. Ultrathin sections (60 nm) were cut and mounted on copper grids. Sections were stained using uranyl acetate and lead citrate. Backscattered scanning electron microscopy (BSEM) was used to quantify the osteocyte lacunar area, as described previously (37).

Serum analysis

The serum concentrations of bone-specific collagen degradation products (CTX-1), Sost, Fgf23, PTH and Rankl were determined by ELISA (Immunodiagnostic Sytems, #AC-06F1; R&D systems, #MSST00; Kainos Laboratories, #CY-4000; Immutopics, #60-2305; R&D systems, #MTR00). Serum phosphorus was measured by the phosphomolybdate technology (Stanbio Laboratory, #0830).

Treatment by ERT

Mice received weekly intravenous injection of Naglazyme® at a dose of 1 mg/kg and in a volume of 150 µl, similar to what was been reported previously (38). Treatment was performed from 12 to 24 weeks of age. Littermate mice were allocated randomly to treatment groups, and endpoint measurements (µCT and histomorphometry) were performed in a blinded fashion. No unexpected or severe adverse events were observed.

Human bone biopsy specimen

A transiliac crest biopsy was taken, with informed consent of the parents, during orthopedic surgery from a 13 years old boy with MPS-VI, who received ERT starting at 9 years of age. The biopsy specimen was embedded undecalcified into methylmetacrylate. Sections were stained by toluidine blue, von Kossa/van Gieson and Goldner staining procedures, as described (29). Histomorphometric analysis was performed using the OsteoMeasure system. The values were set into relation to the values measured in age-matched control biopsies from our previously published archive (39).

Data analysis

When comparing two groups, significance was calculated using unpaired, two-tailed Student's t test (Microsoft Excel®). When comparing more than two groups, significance was calculated by one-way analysis of variance (ANOVA) with Tukey *post hoc* analysis (Graph Pad Prism®). No statistical method was used to predetermine sample size. All data are presented as mean + standard deviations. Statistical significance indicated by *P* value (**P*<0.05, ***P*<0.005, ****P*<0.0005).

Results

Acp2 and Acp5 synergize in bone resorption and Ctsk activation

Since we have previously reported that the moderate osteopetrotic phenotype of *Acp5*-deficient mice is enhanced by additional deficiency of *Acp2* (15), we analyzed the bone phenotype of wildtype, *Acp2*$^{-/-}$, *Acp5*$^{-/-}$ and *Acp2/Acp5*$^{-/-}$ littermates by micro-computed tomography (µCT) (Fig. 1A,B). We found that femoral length and trabecular bone mass, but not cortical thickness, were significantly more affected in *Acp2/Acp5*$^{-/-}$ mice compared with single deficiency littermates, suggesting synergistic action of the two acid phosphatases in bone resorption (Fig. 1C; Suppl. Fig. S1A). To confirm this hypothesis we plated primary bone marrow cells from mice of the respective genotypes on dentin chips and differentiated them into osteoclasts (Fig. 1D,E). Although *Acp5*$^{-/-}$ and *Acp2/Acp5*$^{-/-}$ cells were negative in TRAP staining, we did not observe significant differences in the number or size of osteoclasts, yet the *ex vivo* resorptive activity was specifically impaired in *Acp2/Acp5*$^{-/-}$ cultures (Fig. 1F; Suppl. Fig. S1B,C). By qRT-PCR we found that *Ctsk* was transcriptionally activated in *Acp2/Acp5*$^{-/-}$ osteoclasts, in contrast to *Clcn7*, encoding the lysosomal $2Cl^-/H^+$ exchanger Clc-7, which is required for acidification of the resorption lacuna (Fig. 1G) (13). Importantly however, the enzymatic activity of Ctsk was significantly reduced in *Acp2/Acp5*$^{-/-}$ osteoclasts, suggesting an impairment of Ctsk function (Fig. 1H).

In various tissues, Acp2 and Acp5 were found to be essential for dephosphorylation of M6P targeting signals on lysosomal enzymes upon arrival in lysosomes (36, 40). Since Ctsk has a calculated isoelectric point (pI) of 8.6, in contrast to the majority of lysosomal enzymes with a pI in the acidic range, we hypothesized that its impaired activity in *Acp2/Acp5*$^{-/-}$ osteoclasts is related to an altered protein charge. Indeed, when we performed two-dimensional gel electrophoresis followed by Ctsk western blotting we observed a shift of Ctsk towards a more acidic pH in *Acp2/Acp5*$^{-/-}$ osteoclasts (Fig. 1I). Moreover, western blotting using an M6P-specific single-chain antibody revealed that M6P-containing proteins were most abundant in cell

lysates from *Acp2/Acp5*$^{-/-}$ osteoclasts (Suppl. Fig. S2A). These data suggested that Acp2 and Acp5 are required for M6P dephosphorylation of lysosomal enzymes in osteoclasts, which is important for Ctsk activity.

Arsb is an osteoclast differentiation marker and a substrate of Acp2/Acp5

The detection of several M6P-containing proteins in *Acp2/Acp5*$^{-/-}$ osteoclasts suggested that additional physiologically relevant substrates of Acp2 and Acp5 might exist (Fig. 2A). This was further supported by electron microscopy, where we found that *Acp2/Acp5*$^{-/-}$ osteoclasts displayed accumulation of electron-lucent lysosomal structures, which were not detected in osteoclasts of *Ctsk*-deficient mice (Suppl. Fig. S2B). With the aim to identify other lysosomal enzymes expressed in differentiated osteoclasts, we utilized an unbiased approach, i.e. Affymetrix Gene Chip hybridization. Here we compared four stages during *ex vivo* osteoclastogenesis of wildtype bone marrow cells, thereby identifying *Calcr* (encoding the calcitonin receptor) (41) as the most strongly induced transcript between day 1 and day 7 of differentiation (Fig. 2B). With respect to lysosomal enzymes we observed the highest induction of *Ctsk, Acp5* and *Arsb*, the latter also being three-fold induced between day 4 and 5, after addition of M-Csf and Rankl (Fig. 2C).

To analyze if Arsb is dephosphorylated by Acp2 and Acp5 we incubated wildtype and *Acp2/Acp5*$^{-/-}$ osteoclasts with recombinant human ARSB for 4 hours and observed a similar uptake rate and lysosomal processing to the mature form regardless of the genotype (Fig. 2D). Importantly however, the lysosomal form of ARSB still contained M6P residues in *Acp2/Acp5*$^{-/-}$ cultures, but exhibited significantly reduced enzymatic activity compared to wildtype cells (Fig. 2E). Likewise, the endogenous activity of Arsb was strongly reduced in *Acp2/Acp5*$^{-/-}$ osteoclasts despite increased mRNA levels, whereas decreased activities of the lysosomal enzymes ß-galactosidase (Glb1), α-mannosidase (Man2b1) and ß-glucuronidase (Gusb) were associated with reduced mRNA levels (Fig. 2F). Taken together, these experiments identified Arsb as a

further lysosomal osteoclast differentiation marker, whose activity, similar to Ctsk, depends on dephosphorylation by Acp2 and Acp5.

High trabecular bone mass in Arsb-deficient mice

Although MPS-VI patients with *ARSB* mutations are characterized by various abnormalities of skeletal growth and development, the function of Arsb in bone remodeling cell types is still unknown. By qRT-PCR we found that *Arsb* is highly expressed in kidney, bone and cultured osteoclasts (Fig. 3A), which led us to analyze a mouse model (thereafter termed *Arsb*$^{m/m}$) carrying a nonsense mutation in the *Arsb* gene (c.379G>T), leading to a truncated protein (p.Glu127*) lacking the catalytic domain (42). These mice displayed shortening of all skeletal elements as a consequence of growth plate abnormalities, where epiphyseal chondrocytes, similar to articular chondrocytes, were characterized by lysosomal storage accumulation (Suppl. Fig. S3). At 12 weeks of age *Arsb*$^{m/m}$ mice additionally displayed a high bone mass phenotype, as evidenced by contact Xray (Fig. 3B) and undecalcified histology (Fig. 3C). Moreover, as assessed by µCT, we found that *Arsb*$^{m/m}$ had shortened femora, but also displayed increased trabecular bone mass compared to wildtype littermates (Fig. 3D).

Histologically, we detected numerous cartilage remnants in spine sections from *Arsb*$^{m/m}$ mice, indicative of an osteopetrotic phenotype (Fig. 3E). We additionally observed that osteoclasts and osteocytes appeared enlarged in *Arsb*$^{m/m}$ sections, although eroded bone surfaces were present (Fig. 3F). Histomorphometric quantification revealed that the osteoclast surface per bone surface (OcS/BS) was not significantly different between 12 weeks old wildtype and *Arsb*$^{m/m}$ littermates, and the same was the case for serum CTX-1 levels as readout for bone resorption (Fig. 3G). Taking into account however, that the total number of osteoclasts, given their high bone mass phenotype, is increased in *Arsb*$^{m/m}$ mice, this finding suggested that the resorptive activity of individual osteoclasts is impaired by Arsb deficiency. To support this hypothesis we additionally determined Acp5 activities in the serum (to normalize for osteoclast

number) and found that the Acp5/CTX-1 ratio was indeed reduced in *Arsb*$^{m/m}$ mice (Fig. 3H). Overall these results supported our hypothesis that Arsb is required for osteoclast activity, although the osteopetrotic phenotype is less severe than reported for other mouse models (11-14).

The resorption defect of Arsb-deficient osteoclasts is corrected by mannose-dependent uptake of recombinant ARSB

Similar to what was observed in *Acp2/Acp5*$^{-/-}$ mice, lysosomal storage accumulation was also detected in *Arsb*$^{m/m}$ osteoclasts by electron microscopy (Fig. 4A). Consistently, we detected increased immunoreactivity for the lysosome-associated membrane protein Lamp1 in primary *Arsb*$^{m/m}$ osteoclasts (Fig. 4B). That lysosome biogenesis is not diminished by Arsb deficiency was supported by western blotting and activity assays for specific lysosomal proteins, where we only observed the expected loss of Arsb activity in mutant cultures (Fig. 4C,D). We also compared osteoclastogenesis and dentin resorption of wildtype and *Arsb*$^{m/m}$ osteoclasts. Whereas the number of osteoclasts was not different between the genotypes, *Arsb*$^{m/m}$ osteoclasts displayed significantly reduced resorptive activity (Fig. 4E). Importantly, this deficit of *Arsb*$^{m/m}$ cells could be corrected, when the cells were cultured in the presence of recombinant human ARSB.

The lysosomal delivery and M6P dephosphorylation of ARSB in *Arsb*$^{m/m}$ osteoclasts was demonstrated by western blotting using ARSB- and M6P-specific antibodies (Fig. 5A). Interestingly, whereas the endocytosis of recombinant ARSB by M6P receptors at the cell surface is the rationale for ERT in MPS-VI (23, 24), we unexpectedly observed that ARSB uptake was strongly inhibited by a molar excess of mannose, but only marginally by M6P (Fig. 5B). Together with the differential expression of the mannose receptors *Mrc1* and *Mrc2* during osteoclastogenesis (Fig. 5C), these data revealed that osteoclasts internalize ARSB in an M6P-independent manner. Most importantly however, our collective findings demonstrated that Arsb

deficiency impairs the activity of bone-resorbing osteoclasts, thereby causing a moderate osteopetrotic phenotype.

Lysosomal storage in Arsb-deficient osteocytes does not fully impair their functions

By electron microscopy we additionally found that *Arsb*$^{m/m}$ osteoblasts displayed lysosomal storage accumulation (Fig. 6A), which was even more pronounced in the terminally differentiated osteocyte population (Fig. 6B). Of note, we did not observe these abnormalities in *Acp2/Acp5*$^{-/-}$ mice, although ARSB uptake assays demonstrated that Acp2 and Acp5 are also required for dephosphorylation of M6P residues on ARSB in primary osteoblasts (Fig. 6C). To address the possibility that the high trabecular bone mass phenotype of *Arsb*$^{m/m}$ mice is partially explained by an activation of osteoblast function, we applied cellular and dynamic histomorphometry. Neither osteoblast surface and bone formation rate per bone surface (ObS/BS and BFR/BS), nor the mineral apposition rate (MAR) were different between 12 weeks old wildtype and *Arsb*$^{m/m}$ littermates (Fig. 6D). We additionally analyzed the osteogenic capacity of primary calvarial osteoblasts and found that *Arsb*$^{m/m}$ cells differentiated *ex vivo* for 20 days displayed moderately reduced matrix mineralization (Fig. 6E). These data show that the high trabecular bone mass phenotype of *Arsb*$^{m/m}$ mice is not explained by an activation of osteoblast function.

Since osteocytes control skeletal remodeling and serum phosphate homeostasis by the production of specific proteins, i.e. Sost and Fgf23 (43, 44), it was important to assess, if the lysosomal storage accumulation in *Arsb*$^{m/m}$ osteocytes impairs these functions. By qRT-PCR we observed reduced mRNA expression of *Arsb*, but not of marker genes for osteoblasts (*Bglap, Ibsp*) or osteocytes (*Sost, Phex, Dmp1*) in *Arsb*$^{m/m}$ femoral bones (Fig. 7A). Consistently, serum concentrations of Sost were not different between 12 weeks old wildtype and *Arsb*$^{m/m}$ littermates, and their elevation in 24 weeks old *Arsb*$^{m/m}$ mice is readily explained by the higher bone mass of these animals (Fig. 7B). We also determined the serum concentrations of Rankl

and PTH, yet in both cases we did not observe significant differences between the two groups (Suppl. Fig. S4).

Since expression of *Fgf23* is barely detectable under physiological conditions, we crossed *Arsb*$^{m/m}$ mice with Phex-deficient *Hyp* mice, displaying hypophosphatemia caused by transcriptional activation of *Fgf23* (45). Our analyses of wildtype, *Arsb*$^{m/m}$, *Hyp*$^{+/d}$ and *Arsb*$^{m/m}$;*Hyp*$^{+/d}$ littermates revealed that the severe osteocyte pathology caused by Arsb deficiency did not influence the *Hyp* phenotype. More specifically, we observed severe osteoid enrichment in both, *Hyp*$^{+/d}$ and *Arsb*$^{m/m}$;*Hyp*$^{+/d}$ mice (Fig. 7C). Consistently, excess production of Fgf23 and hypoposphatemia in *Hyp* mice was not influenced by Arsb deficiency (Fig. 7D). Taken together, these data do not only demonstrate that the majority of osteocytes in *Arsb*$^{m/m}$ mice are able to produce relevant regulatory proteins, they also show that GAG degradation in osteocytes depends on the activity of Arsb.

Systemic delivery of ARSB corrects trabecular bone pathologies in Arsb-deficient mice

We next addressed the question, if ERT would correct trabecular bone pathologies in *Arsb*$^{m/m}$ mice. We therefore administered recombinant human ARSB by weekly intravenous injection at a dose of 1 mg/kg (38). The treatment was started in 12 weeks old mice until the analysis was performed at 24 weeks of age. By quantifying bone lengths on contact Xrays we found that the length reduction of *Arsb*$^{m/m}$ bones was not corrected by ERT (Fig. 8A). We also did not observe an ERT influence on epiphyseal chondrocytes, since the growth plate width was still increased in treated *Arsb*$^{m/m}$ mice (Fig. 8B). Since MPS-VI patients typically display craniofacial bone abnormalities, which are not obviously affected by ERT, we further quantified enlargement of the jawbones by µCT (Fig. 8C). Here we observed significant jaw exostosis in *Arsb*$^{m/m}$ mice, which was however unaffected by the treatment (Fig. 8D).

Importantly however, undecalcified histology and subsequent histomorphometry clearly demonstrated a treatment effect in the trabecular bone compartment (Fig. 9A). More

specifically, quantification of the bone volume per tissue volume (BV/TV) in spine and tibia sections revealed that the high trabecular bone mass phenotype of *Arsb*$^{m/m}$ mice was fully normalized by ERT (Fig. 9B). A strong therapeutic impact of systemic ARSB delivery was also found with respect to the osteocyte population. We observed that *Arsb*$^{m/m}$ mice displayed overall enlarged osteocyte lacunae, some of these without visible nuclei in undecalcified sections stained with toluidine blue (Fig. 9C,D). Although electron microscopy demonstrated that all of these lacunae contained osteocytes with strikingly enlarged, electron-lucent lysosomes, the quantification of these apparently empty osteocyte lacunae was an ideal readout for the influence of ERT on the osteocyte network. In fact, the increased number of apparently empty osteocyte lacunae in the trabecular bone of *Arsb*$^{m/m}$ mice was fully normalized by ERT (Fig. 9E), which was supported by electron microscopy (Suppl. Fig. S5). In contrast, *Arsb*$^{m/m}$ osteocytes in cortical bone were not affected by the treatment, a discrepancy best explained by the higher rate of skeletal remodeling in the trabecular bone compartment.

To directly analyze the influence of ERT on the osteocyte lacunar area we additionally applied backscattered scanning electron microscopy (BSEM) (Fig. 9F). Here we observed increased values in trabecular and cortical bone of untreated *Arsb*$^{m/m}$ mice, which were normalized by ERT only in the trabecular compartment (Fig. 9G). Similar findings were obtained through analysis of an iliac crest biopsy from a 13 years old boy with MPS-VI, who received ERT for 4 years. Here we found, that the bone volume per tissue volume was not elevated compared to 5 iliac crest bone biopsies from skeletal-intact donors (14.8 + 2.9 years of age). Importantly, the osteocyte lacunar area in the patient´s biopsy was specifically increased in the cortical bone compartment (Suppl. Fig. S6).

One of the clinically relevant complications in MPS-VI patients is cervical cord compression, which often requires surgery (46). Since it is still debated, if ERT can influence this pathology, we finally quantified the width of the vertebral body C1 in the different groups of untreated and ERT-treated mice (Fig. 9H). We found that the C1 width was significantly

reduced in 24 weeks old *Arsb*$^{m/m}$ mice and that ERT prevented this phenotype (Fig. 9I). These latter findings essentially demonstrate that cervical cord compression is a consequence of impaired bone remodeling. Moreover, our collective findings revealed that all trabecular bone pathologies of *Arsb*$^{m/m}$ mice, including the osteopetrotic phenotype, are fully normalized by ERT.

Discussion

Lysosome dysfunctions are often associated with skeletal manifestation, yet the cellular and molecular bases are poorly understood. The essential role of lysosomes for bone resorption was principally established, especially since Ctsk and Acp5 are long known as osteoclast differentiation marker proteins. Almost all newly synthesized lysosomal enzymes are transported from the Golgi apparatus to lysosomes in an M6P-dependent manner (16). M6P residues are generated by GlcNAc-1-phosphotransferase (encoded by the *GNPTAB* gene), whose loss-of-function causes mucolipidosis type II (ML-II), associated with hypersecretion of lysosomal enzymes (47). The impact of *Gnptab* deficiency on osteoclast function was first demonstrated by ultrastructural analysis of primary osteoclasts, where it was found that *Gnptab*-deficient cells display defective lysosomal targeting and hypersecretion of Ctsk and Acp5 (48). We have previously studied the skeletal phenotype of a *Gnptab*-knockin mouse model of ML-II, where we identified an osteoporotic phenotype primarily explained by a higher number of functionally active osteoclasts (49). Supported by *ex vivo* studies these findings strongly suggested that the lack of M6P-dependent lysosomal targeting does not fully impair bone resorption. Although Acp5 was shown to mediate M6P dephosphorylation in many cell types, its mechanism of action in osteoclasts was still undefined. In the present study we followed up on previous data (15) and utilized mouse deficiency models to demonstrate that Acp2 and Acp5 synergistically activate osteoclast-mediated bone resorption *in vivo* and *in vitro*. We additionally show that Acp2 and Acp5 are required for M6P dephosphorylation of lysosomal enzymes in osteoclasts, which is a prerequisite for maximum Ctsk activity in the acidified lumen of lysosomes. Using an unbiased approach we identified other genes encoding lysosomal enzymes with differential expression in primary osteoclasts and putative function in bone resorption. One of these enzymes was Arsb, whose functional analysis in bone remodeling cell types was the primary focus of the present study.

Arsb (N-acetylgalactosamine-4-sulfatase) is required to hydrolyze sulfate esters from specific GAG types, i.e. CS and DS. *ARSB* mutations are the cause of MPS-VI, also known as Maroteaux-Lamy syndrome, a rare but prototypical lysosomal storage disorder associated with lysosomal GAG accumulation in various cell types (50). Clinically, individuals with MPS-VI are mostly affected by skeletal abnormalities (dysostosis multiplex), which include impaired skeletal growth, craniofacial bone deformities and functional impairment of the joints (22). Additional complications include hepatosplenomegaly, cardiac anomalies and corneal clouding, yet the central nervous system is not affected. Until now, there are only few studies focusing on the putative role of Arsb in bone cells. It was shown that the targeted deletion of *Arsb* in mice causes some obvious skeletal abnormalities, as shown by Xray, together with subtle differences in craniofacial bones, i.e. decreased skull length (51). There are also conflicting data on the trabecular bone mass in vertebral bodies, which was found to be increased in a rat model of MPS-VI, but reduced in a feline model of the disease (52, 53). In the present study we utilized a mouse model carrying a nonsense mutation in exon 2 of the *Arsb* gene, which results in a truncated and inactive protein. Through the direct comparison of all parameters between $Arsb^{m/m}$ mice and their corresponding wildtype littermates we observed increased trabecular bone mass in vertebral bodies and long bones of $Arsb^{m/m}$ mice at the ages of 12 and 24 weeks. Since $Arsb^{m/m}$ mice additionally displayed key features of dysostosis multiplex, we regarded them as a valuable tool to study the impact of Arsb deficiency on different skeletal cell types.

By a combination of bone-specific histomorphometry and cell culture experiments we were able to show that the high bone mass phenotype of $Arsb^{m/m}$ mice is a consequence of impaired osteoclast activity. Primary osteoclasts from wildtype and $Arsb^{m/m}$ mice were able to endocytose and proteolytically activate recombinant human ARSB in an M6P-independent manner. Of note, mannose-dependent uptake into macrophages has also been shown for other lysosomal enzymes, i.e. ß-glucocerebrosidase and acid sphingomyelinase, mutated in Gaucher and Niemann-Pick-A/B disease, respectively (54, 55). Since macrophages and osteoclasts are

derived from a common hematopoietic progenitor, these findings indicate that their lysosomal enzyme uptake is mediated by mannose receptors rather than M6P receptors as described for other cell types. We additionally found that endocytosed and proteolytically processed ARSB in *Acp2/Acp5*-deficient osteoclasts still contained M6P residues. The concomitant decrease of endocytosed ARSB activity in *Acp2/Acp5*-deficient osteoclasts, as well as of endogenous Arsb activity, demonstrates that M6P dephosphorylation by Acp2 and Acp5 is conducive for Arsb activity in osteoclasts. Thus, our data provide the first evidence that M6P residues do not only serve as a targeting signal for lysosomal enzymes, but that immediate M6P removal upon arrival in lysosomes by Acp2 and Acp5, is a requisite for full enzymatic activity, as shown here for Ctsk and Arsb, to guarantee lysosome function.

Of note, although M6P residues were not dephosphorylated in *Acp2/Acp5*-deficient primary osteoblasts either, we did not observe lysosomal storage accumulation in *Acp2/Acp5*-deficient osteoblasts or osteocytes *in vivo*, unlike it was the case in Arsb-deficient mice. One possible explanation for the differential impact of *Acp2/Acp5*- and Arsb deficiency on bone remodeling cell types is that bone resorption and matrix degradation largely depends on lysosomal activities, whereas osteocytic lysosomes may be less relevant for the cellular catabolism. Therefore, a residual Arsb activity (as a consequence of *Acp2/Acp5*-deficiency) might be sufficient to ensure the cellular turnover of GAG-carrying proteins in osteocytes, whereas a complete Arsb deficiency might cause lysosomal storage in this long-lived cell population. It remains to be established, if the storage material in Arsb-deficient osteocytes is primarily derived from intracellular proteins or cell-associated proteoglycans, or if Arsb participates in osteocyte-mediated bone matrix turnover. This question is best addressed by future experiments, where the response of wildtype and *Arsb*-deficient mice could be compared under conditions of calcium stress, which induce a process known as osteocytic osteolysis (56). In any case, it is important to state that the severe lysosomal storage accumulation in *Arsb*-

deficient osteocytes did not impair their major functions in controlling bone remodeling or phosphate homeostasis, at least until the age of 24 weeks.

The observed correction of the *ex vivo* defect of *Arsb*$^{m/m}$ osteoclasts by exogenous ARSB additionally led us to analyze the clinically relevant question, whether ERT would correct the osteopetrotic phenotype of *Arsb*$^{m/m}$ mice. ERT has been established as a leading treatment option for certain lysosomal storage disorders, including MPS-I, MPS-II and MPS-VI (23, 24). Until now it is still undefined, if potential defects of osteoblasts, osteoclasts and/or osteocytes in individuals with MPS are influenced by ERT, yet it was hypothesized that the skeleton is less accessible to systemically delivered recombinant enzymes in comparison to non-mineralized tissues (57). Therefore, since we observed a remarkable influence of ERT on the bone remodeling phenotype of *Arsb*$^{m/m}$ mice, our combined data can be regarded as an important proof-of-principle demonstrating that systemically delivered lysosomal enzymes can reach and enter bone remodeling cell types to correct their respective defects, at least in the case of MPS-VI. These findings are not fully unexpected, as bone is a highly vascularized tissue with bone remodeling being controlled by various endocrine regulators (58). On the other hand, it was remarkable to observe that even the severe defects of *Arsb*$^{m/m}$ osteocytes were corrected by ERT, albeit in a compartment-specific manner. The differential impact of ERT on trabecular and cortical osteocytes is best explained by the higher remodeling rate in the trabecular compartment (59). Since osteocytes are terminally differentiated osteoblasts, their *de novo* generation in the presence of systemically delivered ARSB most likely prevents lysosomal GAG storage and enlargement of the osteocyte lacunar area. In cortical bone however, existing osteocytes are not continuously replaced, and therefore no ERT-mediated reduction of the osteocyte lacunar area was observed.

In our opinion, the data obtained by analysis of *Arsb*$^{m/m}$ mice are not only interesting from a basic scientific perspective, they should also be considered as clinically relevant, at least for individuals with MPS-VI. First, they do not only show that bone remodeling in *Arsb*$^{m/m}$ mice

can be normalized by ERT, but also that ERT can prevent cervical cord compression, one of the most serious complications in MPS-VI patients. Importantly, there is still no consensus about the efficacy of ERT in terms of cervical cord compression, since there was no consistent monitoring of the respective individuals before the treatment was initiated (46). Second, while the pathological features of bone remodeling cell types in *Arsb*$^{m/m}$ mice were corrected by ERT, the cartilage-associated phenotypes (growth plate widening, bone length reduction) were not. It is established that skeletal growth and development largely depend on coordinated chondrocyte differentiation processes (60). Therefore, the common observation that key aspects of dysostosis multiplex (impaired skeletal growth, articular cartilage thickening) are not remarkably influenced by ERT is explained to a large extend by failure to correct chondrocyte-specific defects. It is likely that this failure is attributable to the avascular nature of cartilaginous tissues, but it is also possible that chondrocytes have reduced capacity to endocytose recombinant lysosomal enzymes. The *Arsb*$^{m/m}$ mice provide an excellent tool to address these questions, yet this requires additional studies, where the treatment has to be initiated in growing animals.

In conclusion, by applying an unbiased approach to screen for lysosomal enzymes with a putative role in bone resorption, we identified Arsb as a key enzyme with a physiologically relevant function in skeletal turnover. We demonstrated that bone remodeling cell types are accessible to systemically delivered ARSB, and that ERT fully corrects all trabecular bone pathologies of *Arsb*$^{m/m}$ mice. It is now required to deepen the analysis of MPS-VI patients, comparing baseline and post-treatment pathologies, including parameters of bone remodeling. In addition, it should be addressed if the findings of the present study are specific for MPS-VI, or if they are of general relevance for all lysosomal storage disorders with skeletal manifestation.

Acknowlegdements

The authors thank Johannes Brand, Nicole Lueder, Andrea Nitsche, Gudrun Arndt, Chudamani Raithore, Emanuela Szpotowicz and Sandra Perkovic for expert technical assistance. The research leading to these results has received funding from the European Community's Seventh Framework Programme under grant agreement n°602300 (SYBIL), from the European Union's Horizon 2020 research and innovation program under the Marie Sklodowska-Curie grant agreement No 794386, and from grants by the Deutsche Forschungsgemeinschaft (AM 103/25-1, SCHI 504/8-1, PO 1539/1-1, SFB877).

Authors' roles: Study design: SP, MA, TB and TS. Study conduct: TS. Data collection: AA, SP, AJ, TAY, GM, AS, SCK, TR, MS, TK, MN, OW, RVV, JA, JMP, CB, SB, CP. Data analysis: SP, RS, NM, TMC, PS, AR, TS. Data interpretation: SP, MA, TB and TS. Drafting manuscript: SP, TB and TS.

References

1. Boyce BF. Advances in the regulation of osteoclasts and osteoclast functions. J Dent Res. 2013;92(10):860-7.
2. Cappariello A, Maurizi A, Veeriah V, Teti A. The Great Beauty of the osteoclast. Arch. Biochem. Biophys. 2014;55870-8.
3. Ferron M, Settembre C, Shimazu J, et al. A RANKL-PKCbeta-TFEB signaling cascade is necessary for lysosomal biogenesis in osteoclasts. Genes Dev. 2013;27(8):955-69.
4. Costa AG, Cusano NE, Silva BC, Cremers S, Bilezikian JP. Cathepsin K: its skeletal actions and role as a therapeutic target in osteoporosis. Nat. Rev. Rheumatol. 2011;7(8):447-56.
5. Hayman AR. Tartrate-resistant acid phosphatase (TRAP) and the osteoclast/immune cell dichotomy. Autoimmunity. 2008;41(3):218-23.
6. Hayman AR, Jones SJ, Boyde A, et al. Mice lacking tartrate-resistant acid phosphatase (Acp 5) have disrupted endochondral ossification and mild osteopetrosis. Development. 1996;122(10):3151-62.
7. Bune AJ, Hayman AR, Evans MJ, Cox TM. Mice lacking tartrate-resistant acid phosphatase (Acp 5) have disordered macrophage inflammatory responses and reduced clearance of the pathogen, Staphylococcus aureus. Immunology. 2001;102(1):103-13.
8. Esfandiari E, Bailey M, Stokes CR, Cox TM, Evans MJ, Hayman AR. TRACP Influences Th1 pathways by affecting dendritic cell function. J Bone Miner Res. 2006;21(9):1367-76.
9. Briggs TA, Rice GI, Daly S, et al. Tartrate-resistant acid phosphatase deficiency causes a bone dysplasia with autoimmunity and a type I interferon expression signature. Nat Genet. 2011;43(2):127-31.
10. Lausch E, Janecke A, Bros M, et al. Genetic deficiency of tartrate-resistant acid phosphatase associated with skeletal dysplasia, cerebral calcifications and autoimmunity. Nat Genet. 2011;43(2):132-7.
11. Yoshida H, Hayashi S, Kunisada T, et al. The murine mutation osteopetrosis is in the coding region of the macrophage colony stimulating factor gene. Nature. 1990;345(6274):442-4.
12. Kong YY, Yoshida H, Sarosi I, et al. OPGL is a key regulator of osteoclastogenesis, lymphocyte development and lymph-node organogenesis. Nature. 1999;397(6717):315-23.
13. Kornak U, Kasper D, Bosl MR, et al. Loss of the ClC-7 chloride channel leads to osteopetrosis in mice and man. Cell. 2001;104(2):205-15.

14. Schinke T, Schilling AF, Baranowsky A, et al. Impaired gastric acidification negatively affects calcium homeostasis and bone mass. Nat Med. 2009;15(6):674-81.
15. Suter A, Everts V, Boyde A, et al. Overlapping functions of lysosomal acid phosphatase (LAP) and tartrate-resistant acid phosphatase (Acp5) revealed by doubly deficient mice. Development. 2001;128(23):4899-910.
16. Braulke T, Bonifacino JS. Sorting of lysosomal proteins. Biochim Biophys Acta. 2009;1793(4):605-14.
17. Clarke LA, Hollak CE. The clinical spectrum and pathophysiology of skeletal complications in lysosomal storage disorders. Best Pract. Res. Clin. Endocrinol. Metab. 2015;29(2):219-35.
18. Parenti G, Andria G, Ballabio A. Lysosomal storage diseases: from pathophysiology to therapy. Annu Rev Med. 2015;66471-86.
19. Cimaz R, La Torre F. Mucopolysaccharidoses. Curr. Rheumatol. Rep. 2014;16(1):389.
20. Wraith JE, Jones S. Mucopolysaccharidosis type I. Pediatr. Endocrinol. Rev. 2014;12 Suppl 1102-6.
21. Gilkes JA, Heldermon CD. Mucopolysaccharidosis III (Sanfilippo Syndrome)- disease presentation and experimental therapies. Pediatr. Endocrinol. Rev. 2014;12 Suppl 1133-40.
22. Vairo F, Federhen A, Baldo G, et al. Diagnostic and treatment strategies in mucopolysaccharidosis VI. Appl. Clin. Genet. 2015;8245-55.
23. Giugliani R, Federhen A, Vairo F, et al. Emerging drugs for the treatment of mucopolysaccharidoses. Expert Opin. Emerg. Drugs. 2016;21(1):9-26.
24. Lachmann RH. Enzyme replacement therapy for lysosomal storage diseases. Curr. Opin. Pediatr. 2011;23(6):588-93.
25. Muenzer J. Early initiation of enzyme replacement therapy for the mucopolysaccharidoses. Mol Genet Metab. 2014;111(2):63-72.
26. Peck SH, Casal ML, Malhotra NR, Ficicioglu C, Smith LJ. Pathogenesis and treatment of spine disease in the mucopolysaccharidoses. Mol Genet Metab. 2016;118(4):232-43.
27. Saftig P, Hunziker E, Wehmeyer O, et al. Impaired osteoclastic bone resorption leads to osteopetrosis in cathepsin-K-deficient mice. Proc. Natl. Acad. Sci. USA. 1998;95(23):13453-8.
28. McLeod MJ. Differential staining of cartilage and bone in whole mouse fetuses by alcian blue and alizarin red S. Teratology. 1980;22(3):299-301.

29. Schulze J, Bickert T, Beil FT, et al. Interleukin-33 is expressed in differentiated osteoblasts and blocks osteoclast formation from bone marrow precursor cells. J Bone Miner Res. 2011;26(4):704-17.
30. Parfitt AM, Drezner MK, Glorieux FH, et al. Bone histomorphometry: standardization of nomenclature, symbols, and units. Report of the ASBMR Histomorphometry Nomenclature Committee. J Bone Miner Res. 1987;2(6):595-610.
31. Kollmann K, Damme M, Markmann S, et al. Lysosomal dysfunction causes neurodegeneration in mucolipidosis II 'knock-in' mice. Brain. 2012;135(Pt 9):2661-75.
32. Saftig P, Hartmann D, Lüllmann-Rauch R, et al. Mice deficient in lysosomal acid phosphatase develop lysosomal storage in the kidney and central nervous system. J Biol Chem. 1997;272(30):18628-35.
33. Di Lorenzo G, Voltolini Velho R, Winter D, et al. Lysosomal proteome and secretome analysis identifies missorted enzymes and their non-degraded substrates in mucolipidosis III mouse cells. Mol Cell Proteomics. 2018;doi: 10.1074/mcp.RA118.000720
34. Zachos C, Blanz J, Saftig P, Schwake M. A critical histidine residue within LIMP-2 mediates pH sensitive binding to its ligand beta-glucocerebrosidase. Traffic. 2012;13(8):1113-23.
35. Müller-Loennies S, Galliciotti G, Kollmann K, Glatzel M, Braulke T. A novel single chain antibody fragment for detection of mannose 6-phosphate-containing proteins: Application in mucolipidosis type II patients and mice. Am J Pathol. 2010;177(1):240-7.
36. Makrypidi G, Damme M, Müller-Loennies S, et al. Mannose 6 dephosphorylation of lysosomal proteins mediated by acid phosphatases Acp2 and Acp5. Mol Cell Biol. 2012;32(4):774-82.
37. Busse B, Hahn M, Soltau M, et al. Increased calcium content and inhomogeneity of mineralization render bone toughness in osteoporosis: mineralization, morphology and biomechanics of human single trabeculae. Bone. 2009;45(6):1034-43.
38. Ferla R, Claudiani P, Cotugno G, Saccone P, De Leonibus E, Auricchio A. Similar therapeutic efficacy between a single administration of gene therapy and multiple administrations of recombinant enzyme in a mouse model of lysosomal storage disease. Hum Gene Ther. 2014;25(7):609-18.
39. Priemel M, von Domarus C, Klatte TO, et al. Bone mineralization defects and vitamin D deficiency: histomorphometric analysis of iliac crest bone biopsies and circulating 25-hydroxyvitamin D in 675 patients. J Bone Miner Res. 2010;25(2):305-12.

40. Sun P, Sleat DE, Lecocq M, Hayman AR, Jadot M, Lobel P. Acid phosphatase 5 is responsible for removing the mannose 6-phosphate recognition marker from lysosomal proteins. Proc. Natl. Acad. Sci. USA. 2008;105(43):16590-5.
41. Keller J, Catala-Lehnen P, Huebner AK, et al. Calcitonin controls bone formation by inhibiting the release of sphingosine 1-phosphate from osteoclasts. Nat. Commun. 2014;55215.
42. Bond CS, Clements PR, Ashby SJ, et al. Structure of a human lysosomal sulfatase. Structure. 1997;5(2):277-89.
43. Balemans W, Van Hul W. Human genetics of SOST. J. Musculoskelet. Neuronal. Interact. 2006;6(4):355-6.
44. Bergwitz C, Jüppner H. FGF23 and syndromes of abnormal renal phosphate handling. Adv. Exp. Med. Biol. 2012;72841-64.
45. Liu S, Zhou J, Tang W, Jiang X, Rowe DW, Quarles LD. Pathogenic role of Fgf23 in Hyp mice. Am. J. Physiol. Endocrinol. Metab. 2006;291(1):E38-49.
46. Solanki GA, Sun PP, Martin KW, et al. Cervical cord compression in mucopolysaccharidosis VI (MPS VI): Findings from the MPS VI Clinical Surveillance Program (CSP). Mol Genet Metab. 2016;118(4):310-8.
47. Kollmann K, Pohl S, Marschner K, et al. Mannose phosphorylation in health and disease. Eur J Cell Biol. 2010;89(1):117-23.
48. van Meel E, Boonen M, Zhao H, et al. Disruption of the Man-6-P targeting pathway in mice impairs osteoclast secretory lysosome biogenesis. Traffic. 2011;12(7):912-24.
49. Kollmann K, Pestka JM, Kühn SC, et al. Decreased bone formation and increased osteoclastogenesis cause bone loss in mucolipidosis II. EMBO Mol Med. 2013;5(12):1871-86.
50. Litjens T, Hopwood JJ. Mucopolysaccharidosis type VI: Structural and clinical implications of mutations in N-acetylgalactosamine-4-sulfatase. Hum Mutat. 2001;18(4):282-95.
51. Evers M, Saftig P, Schmidt P, et al. Targeted disruption of the arylsulfatase B gene results in mice resembling the phenotype of mucopolysaccharidosis VI. Proc. Natl. Acad. Sci. USA. 1996;93(16):8214-9.
52. Frohbergh M, Ge Y, Meng F, et al. Dose responsive effects of subcutaneous pentosan polysulfate injection in mucopolysaccharidosis type VI rats and comparison to oral treatment. PLoS One. 2014;9(6):e100882.

53. Byers S, Nuttall JD, Crawley AC, Hopwood JJ, Smith K, Fazzalari NL. Effect of enzyme replacement therapy on bone formation in a feline model of mucopolysaccharidosis type VI. Bone. 1997;21(5):425-31.
54. Dhami R, Schuchman EH. Mannose 6-phosphate receptor-mediated uptake is defective in acid sphingomyelinase-deficient macrophages: implications for Niemann-Pick disease enzyme replacement therapy. J Biol Chem. 2004;279(2):1526-32.
55. Tekoah Y, Tzaban S, Kizhner T, et al. Glycosylation and functionality of recombinant beta-glucocerebrosidase from various production systems. Biosci. Rep. 2013;33(5):
56. Qing H, Ardeshirpour L, Pajevic PD, et al. Demonstration of osteocytic perilacunar/canalicular remodeling in mice during lactation. J Bone Miner Res. 2012;27(5):1018-29.
57. Harmatz P, Shediac R. Mucopolysaccharidosis VI: pathophysiology, diagnosis and treatment. Front Biosci (Landmark Ed). 2017;22385-406.
58. Niedzwiedzki T, Filipowska J. Bone remodeling in the context of cellular and systemic regulation: the role of osteocytes and the nervous system. J. Mol. Endocrinol. 2015;55(2):R23-36.
59. Feng X, McDonald JM. Disorders of bone remodeling. Annu. Rev. Pathol. 2011;6121-45.
60. Hinton RJ, Jing Y, Jing J, Feng JQ. Roles of Chondrocytes in Endochondral Bone Formation and Fracture Repair. J Dent Res. 2017;96(1):23-30.

Figure Legends

Fig. 1. Acp2 and Acp5 synergize in bone resorption and Ctsk activation. (A) Representative µCT scans of femora from 12 weeks old wildtype (*Acp2*$^{+/+}$/*Acp5*$^{+/+}$), *Acp2*$^{-/-}$, *Acp5*$^{-/-}$ and *Acp2/Acp5*$^{-/-}$ mice. Scale bar, 1 mm. (B) Representative µCT scans of the same femora depicting mineralized bone in red. Scale bar, 100 µm. (C) Quantification of femoral length and trabecular bone volume per tissue volume (BV/TV) in 12 weeks old wildtype (WT), *Acp2*$^{-/-}$, *Acp5*$^{-/-}$ and *Acp2/Acp5*$^{-/-}$ mice (n ≥ 4 mice per genotype). (D) TRAP staining of wildtype, *Acp2*$^{-/-}$, *Acp5*$^{-/-}$ and *Acp2/Acp5*$^{-/-}$ osteoclasts. Scale bar, 25 µm. (E) Dentin resorption by wildtype, *Acp2*$^{-/-}$, *Acp5*$^{-/-}$ and *Acp2/Acp5*$^{-/-}$ osteoclasts. Scale bar, 50 µm. (F) Quantification of osteoclast number (OcN) and resorbed dentin area in the same cultures (n ≥ 5 cultures per genotype). (G) mRNA expression for *Acp2*, *Acp5*, *Ctsk* and *Clcn7* in wildtype and *Acp2/Acp5*$^{-/-}$ osteoclasts (n = 3 cultures per genotype). (H) Relative enzyme activities of Acp2, Acp5 and Ctsk in the same cultures (n ≥ 4 cultures per genotype). (I) Western blot detecting Ctsk (arrows) in cell lysates from wildtype and *Acp2/Acp5*$^{-/-}$ osteoclasts after 2D-SDS-PAGE. Data are presented as mean + s.d. **P*<0.05, ***P*<0.005 and ****P*<0.0005 by one-way analysis of variance (ANOVA) with Tukey *post hoc* analysis (C,F) or two-tailed Student´s t-test (G,H).

Fig. 2. Arsb is an osteoclast differentiation marker and a substrate of Acp2 and Acp5. (A) Western blot of cell lysates from wildtype and *Acp2/Acp5*$^{-/-}$ osteoclasts using an M6P-specific antibody. Calnexin (Canx) was used as a loading control. (B) Schematic presentation of the protocol used for osteoclast differentiation and the four time points subjected to Affymetrix Gene Chip hybridization. Differential expression of *Calcr* is shown below. (C) Heat map showing the signal log ratios (SLR) of genes encoding soluble lysosomal enzymes with increased expression between day 1 and day 7 of osteoclastogenic differentiation (left column). SLR values for day 4 to day 5 are shown in the right column. (D) ARSB and M6P western blot of cell lysates from wildtype (*Acp2*$^{+/+}$/*Acp5*$^{+/+}$) and *Acp2/Acp5*$^{-/-}$ osteoclasts incubated with

ARSB for 4 hours. Precursor and mature forms of ARSB are indicated by closed or open arrowheads, respectively. (E) Arsb activity assays in media (top) or cell lysates (bottom) after 4 hours of ARSB administration (n = 6 cultures per genotype). (F) Relative enzyme activities (top) and mRNA expression (bottom) of Arsb, Hexb (ß-hexosaminidase), Glb1 (ß-galactosidase), Man2b1 (α-mannosidase) and Gusb (ß-glucuronidase) in wildtype and *Acp2/Acp5*$^{-/-}$ osteoclasts (n ≥ 3 cultures per genotype). Data are presented as mean + s.d. **P*<0.05, ***P*<0.005 and ****P*<0.0005 by two-tailed Student´s t-test (E,F).

Fig. 3. Arsb-deficient mice display a moderate osteopetrotic phenotype. (A) *Arsb* expression in different tissues (Li, liver, Sp, spleen, He, heart, Ki, kidney, Lu, lung, Fa, fat, Bo, bone) or cultured bone cells (Obl, osteoblasts, Ocl, osteoclasts) at different stages of differentiation (n = 3 samples per tissue or cell type). (B) Representative contact Xrays of 12 weeks old wildtype and *Arsb*$^{m/m}$ littermates. Scale bar, 5 mm. (C) Kossa/Gieson staining of spine sections from the same mice. Scale bar, 1 mm. (D) Representative µCT scans of femora from the same mice. Scale bar, 100 µm. Quantification of femoral length, trabecular bone volume per tissue volume (BV/TV) and cortical thickness are given on the right (n ≥ 5 mice per genotype). (E) Toluidine blue staining of spine sections reveals the presence of cartilage remnants (arrow) in Arsb-deficient mice. Scale bar, 50 µm. Quantification is given on the right (n ≥ 5 mice per genotype). (F) Toluidine blue staining of spine sections demonstrates the presence of osteoclasts and eroded bone surfaces in wildtype and Arsb-deficient mice, whereas the latter ones also displayed enlarged or apparently empty osteocyte lacunae (arrows). Scale bar, 20 µm. (G) Histomorphometric quantification of the osteoclast surface per bone surface (OcS/BS) and serum CTX-1 levels in 12 weeks old wildtype and *Arsb*$^{m/m}$ mice (n ≥ 4 mice per genotype). (H) Serum Acp5 activities and CTX-1/Acp5 ratios in the same mice (n = 4 mice per genotype). Data are presented as mean + s.d. **P*<0.05, and ****P*<0.0005 by two-tailed Student´s t-test (D,E,G,H).

Fig. 4. Arsb-deficient osteoclasts display a resorption defect. (A) Representative electron microscopy images showing lysosomal storage vacuoles (arrows) in osteoclasts of 12 weeks old *Arsb*$^{m/m}$ mice. Scale bar, 5 µm. (B) Immunofluorescent staining of wildtype and Arsb-deficient osteoclasts with an antibody against the lysosomal membrane protein Lamp1. Nuclei were visualized by DAP staining. Scale bar, 20 µm. (C) Western blot of cell lysates from wildtype and Arsb-deficient osteoclasts using antibodies against the lysosomal proteins Limp2, Lamp1, Clc7 and Ctsk. Calnexin (Canx) was used as a loading control. (D) Enzymatic activities of Arsb, Acp5, ß-hexosaminidase and ß-galactosidase in lysates (left) and media (right) from wildtype and Arsb-deficient osteoclasts ($n \geq 3$ cultures per genotype). (E) Dentin resorption by wildtype and *Arsb*$^{m/m}$ osteoclasts cultured with or without ARSB. Scale bar, 50 µm. Quantification of osteoclast number (OcN) and resorbed dentin area is given on the right (n = 6 cultures per group). Data are presented as mean + s.d. **P*<0.05, and ****P*<0.0005 by two-tailed Student´s t-test (D) or one-way analysis of variance (ANOVA) with Tukey *post hoc* analysis (E).

Fig. 5. Mannose-dependent lysosomal uptake of recombinant ARSB by Arsb-deficient osteoclasts. (A) ARSB and M6P western blot of cell lysates from *Arsb*$^{m/m}$ osteoclasts incubated with ARSB for 4 hours with or without M6P and/or mannose (Man). Precursor and mature forms of Arsb are indicated by closed or open arrowheads, respectively. (B) Arsb activity in cell lysates of wildtype and *Arsb*$^{m/m}$ osteoclasts incubated with ARSB for 4 hours in the absence (-) or presence (+) of M6P and/or mannose (Man) (n = 4 cultures per group). (C) Heat map showing the signal log ratios (SLR) of genes encoding M6P receptors (*M6pr, Igfr2)* and mannose receptors (*Mrc1, Mrc2*) between day 1 and day 7 or between day 4 and day 5 of osteoclastogenic differentiation in wildtype cultures. Signal intensities of *Mrc1* and *Mrc2* at the different time points are shown on the right. Data are presented as mean + s.d. Data represent mean + s.d. ****P*<0.0005 by one-way analysis of variance (ANOVA) with Tukey *post hoc* analysis (B).

Fig. 6. Lysosomal storage in Arsb-deficient osteoblasts and osteocytes. (A) Representative electron microscopy images showing lysosomal storage vacuoles (arrow) in osteoblasts of 12 weeks old *Arsb*$^{m/m}$ mice, which were not observed in 12 weeks old *Acp2/Acp5*$^{-/-}$ mice. Scale bar, 5 µm. (B) Representative electron microscopy images showing lysosomal storage vacuoles in trabecular osteocytes of *Arsb*$^{m/m}$ mice. Scale bar, 5 µm. (C) ARSB and M6P western blot of cell lysates from wildtype and *Acp2/Acp5*$^{-/-}$ osteoblasts (day 20 of differentiation) incubated with ARSB for 4 hours. Precursor and mature forms of ARSB are indicated by closed or open arrowheads, respectively. Calnexin (Canx) was used as a loading control. (D) Histomorphometric quantification of osteoblast surface per bone surface (ObS/BS), bone formation rate per bone surface (BFR/BS) and mineral apposition rate (MAR) in 12 weeks old wildtype and *Arsb*$^{m/m}$ mice ($n \geq 5$ mice per genotype). (E) Alizarin red staining of primary calvarial cultures from wildtype and *Arsb*$^{m/m}$ mice at day 20 of *ex vivo* osteogenic differentiation. Scale bar, 1 cm. Quantification of matrix mineralization is given below (n = 4 cultures per genotype). Data are presented as mean + s.d. $^{**}P<0.005$ by two-tailed Student´s t-test (D,E).

Fig. 7. Arsb-deficient osteocytes are not dysfunctional. (A) mRNA expression of *Arsb*, osteoblast (*Bglap*, *Ibsp*) and osteocyte (*Sost*, *Phex*, *Dmp1*) markers in femoral bones from 12 weeks old wildtype and *Arsb*$^{m/m}$ mice ($n \geq 3$ mice per genotype). (B) Serum Sost concentrations in 12 and 24 weeks old wildtype and *Arsb*$^{m/m}$ mice ($n \geq 3$ per genotype). (C) Kossa/Gieson (top) and toluidine blue (botton) staining of trabecular bone in spine sections from 12 weeks old *Hyp*$^{+/d}$ and *Arsb*$^{m/m}$*;Hyp*$^{+/d}$ littermates. Arrows indicate osteocyte enlargement caused by Arsb-deficiency. Scale bar, 50 µm (top) and 20 µm (bottom). (D) Serum concentrations of Fgf23 and phosphate in the four groups of mice ($n \geq 3$ per genotype). Data are presented as mean + s.d. $^{*}P<0.05$, $^{**}P<0.005$ and $^{***}P<0.0005$ by two-tailed Student´s t-test (A,B) or one-way analysis of variance (ANOVA) with Tukey *post hoc* analysis (D).

Fig. 8. Systemic delivery of ARSB does not correct defects of skeletal growth or development in Arsb-deficient mice. (A) Length of skeletal elements in wildtype, untreated and ERT-treated *Arsb*$^{m/m}$ mice at 24 weeks of age (n ≥ 4 mice per group). (B) Quantification of growth plate (GP) width in tibia sections from the same mice (n ≥ 4 mice per group). (C) Representative µCT images of the jawbones from 24 weeks old wildtype, untreated and ERT-treated *Arsb*$^{m/m}$ mice. The arrow indicates jaw exostosis. Scale bar, 500 µm. (D) Quantification of jaw exostosis in 24 weeks old wildtype, untreated and ERT-treated *Arsb*$^{m/m}$ mice (n ≥ 4 mice per group). Data are presented as mean + s.d. **P*<0.05, ***P*<0.005 and ****P*<0.0005 by one-way analysis of variance (ANOVA) with Tukey *post hoc* analysis (A,B,D).

Fig. 9. Systemic delivery of ARSB corrects trabecular bone pathologies in Arsb-deficient mice. (A) Representative Kossa/Gieson stainings of spine sections from wildtype, untreated and ERT-treated *Arsb*$^{m/m}$ mice at 24 weeks. Scale bar, 1 mm. (B) Quantification of the trabecular bone volume per tissue volume (BV/TV) in spine and tibia sections from the same mice (n ≥ 4 mice per group). (C) Representative toluidine blue staining of trabecular bone demonstrates that enlarged and empty osteocyte lacunae (arrow) were only observed in untreated *Arsb*$^{m/m}$ mice. Scale bar, 50 µm. (D) Representative toluidine blue staining of cortical bone demonstrates that enlarged and empty osteocyte lacunae (arrows) in *Arsb*$^{m/m}$ mice were not affected by the treatment. Scale bar, 50 µm. (E) Number of (apparently) empty osteocyte lacunae per bone area (N.e.L./B.Ar) in trabecular and cortical bone from wildtype, untreated and ERT-treated *Arsb*$^{m/m}$ mice at 24 weeks. (n ≥ 4 mice per group). (F) Backscattered scanning electron microscopy images of trabecular bone from 24 weeks old untreated and ERT-treated *Arsb*$^{m/m}$ mice. Scale bar, 50 µm. (G) Quantification of the lacunar area (Lc.Ar.) in trabecular and cortical bone of the same mice (n ≥ 4 mice per group). (H) Representative µCT images of the cervical cord from 24 weeks old wildtype, untreated and ERT-treated *Arsb*$^{m/m}$ mice. Scale bar, 100 µm. (I) Quantification of C1 width in 24 weeks old wildtype, untreated and ERT-treated *Arsb*$^{m/m}$ mice

(n ≥ 4 mice per group). Data are presented as mean + s.d. *P<0.05, **P<0.005 and ***P<0.0005 by one-way analysis of variance (ANOVA) with Tukey *post hoc* analysis (B,E,G,I).

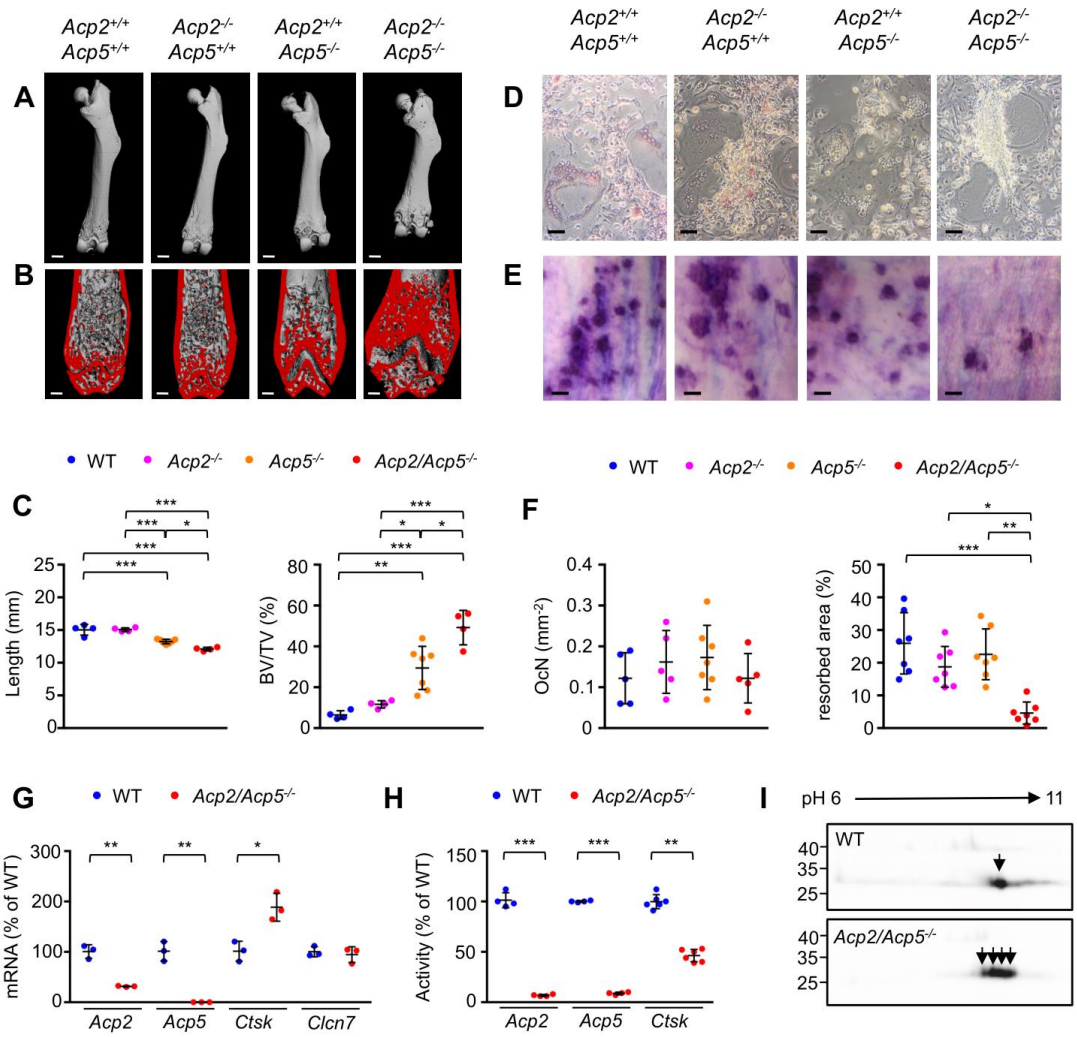

Figure 1

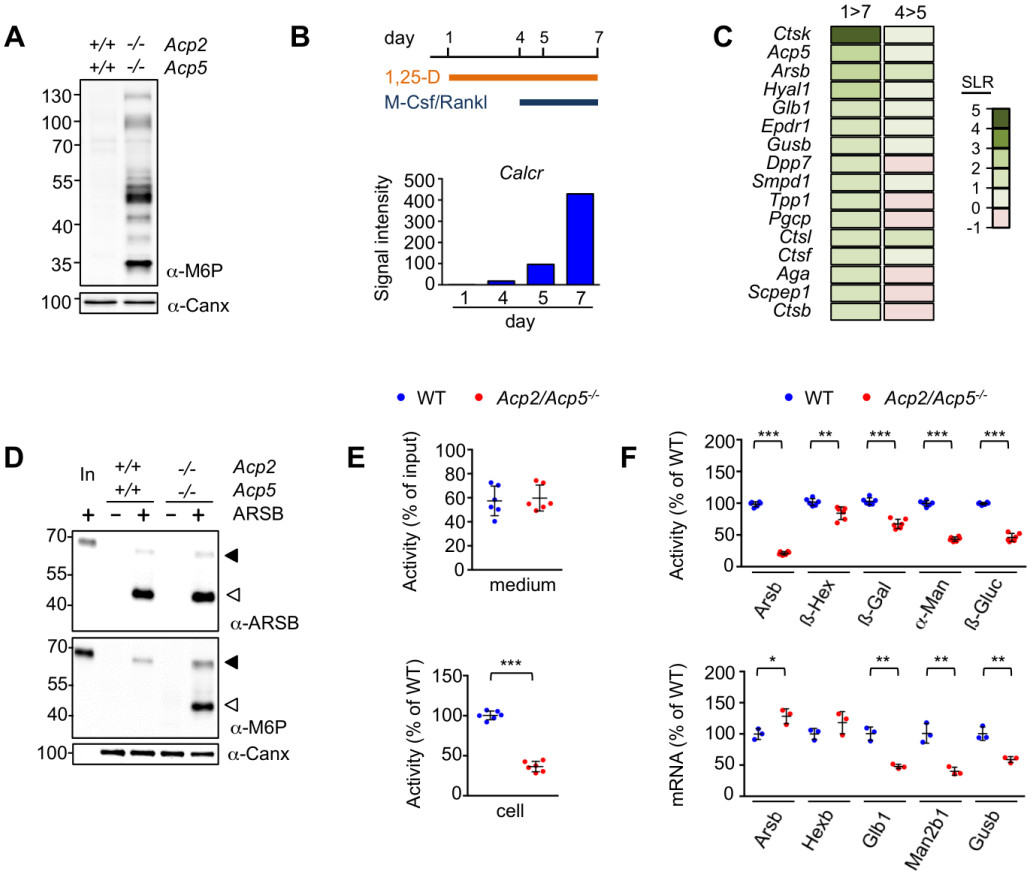

Figure 2

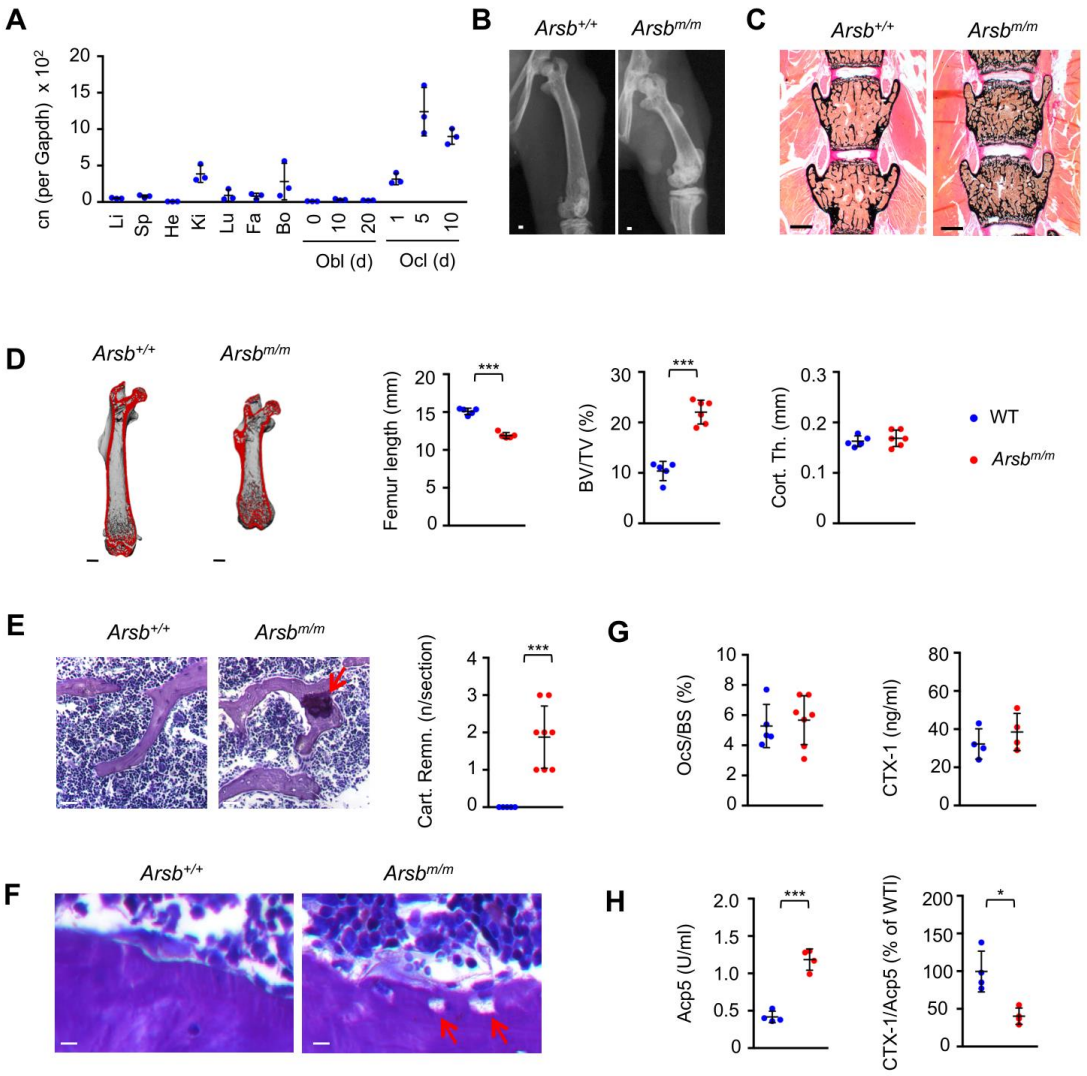

Figure 3

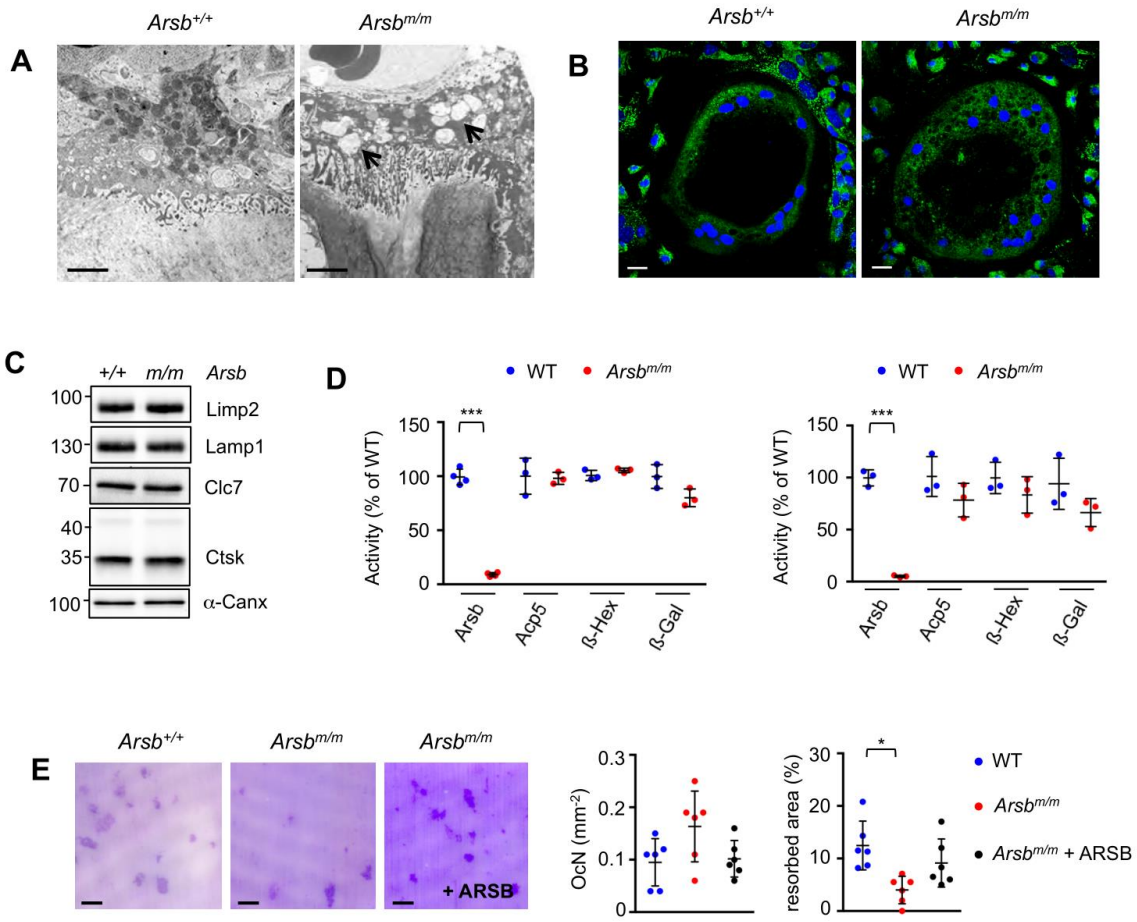

Figure 4

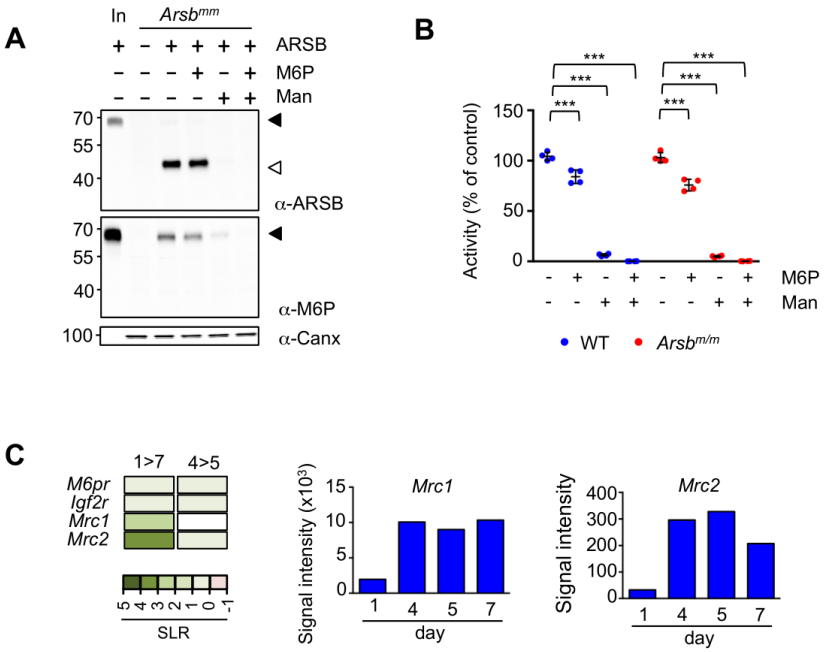

Figure 5

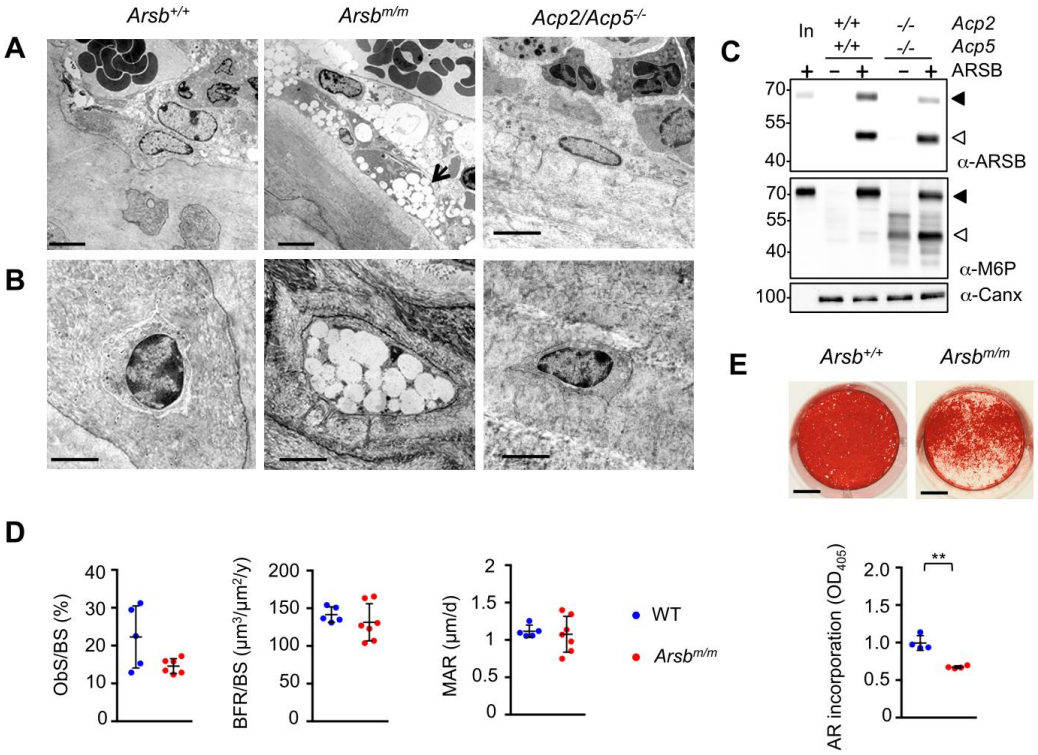

Figure 6

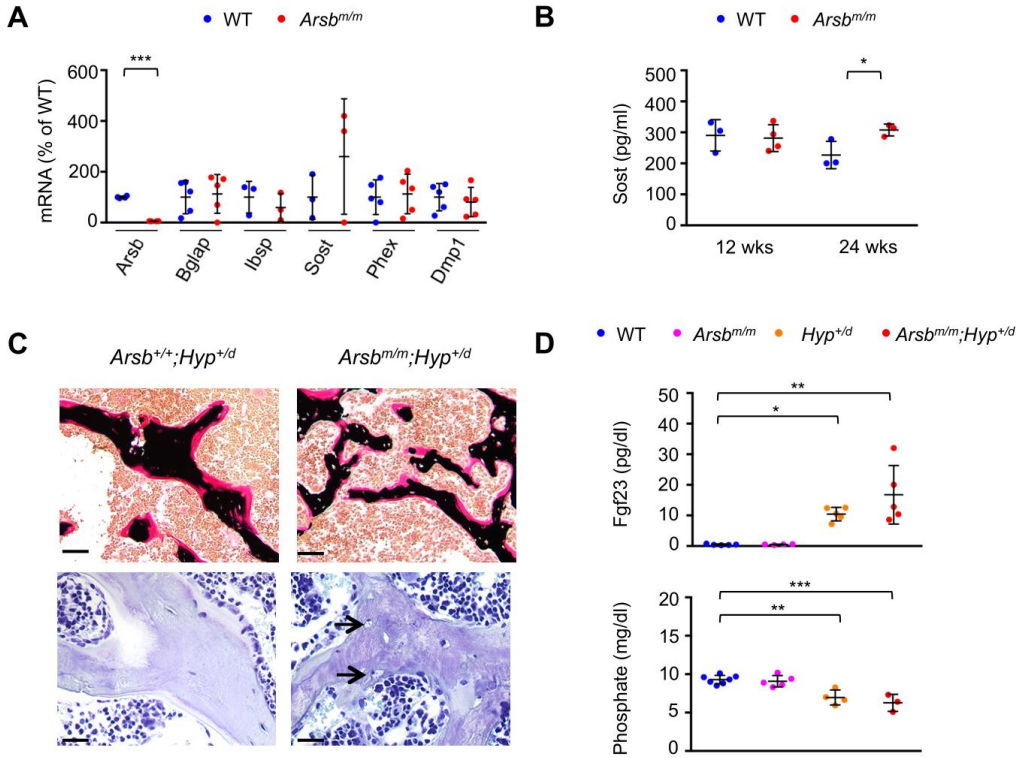

Figure 7

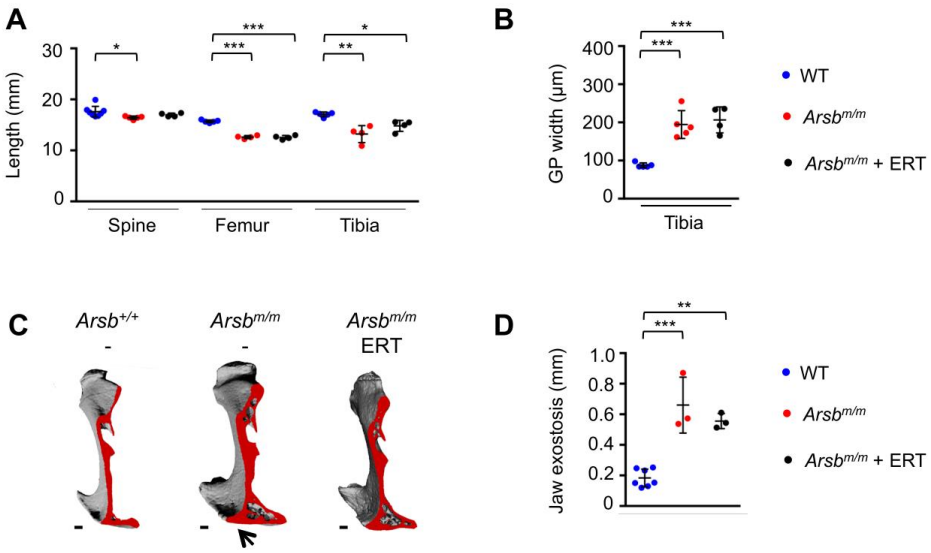

Figure 8

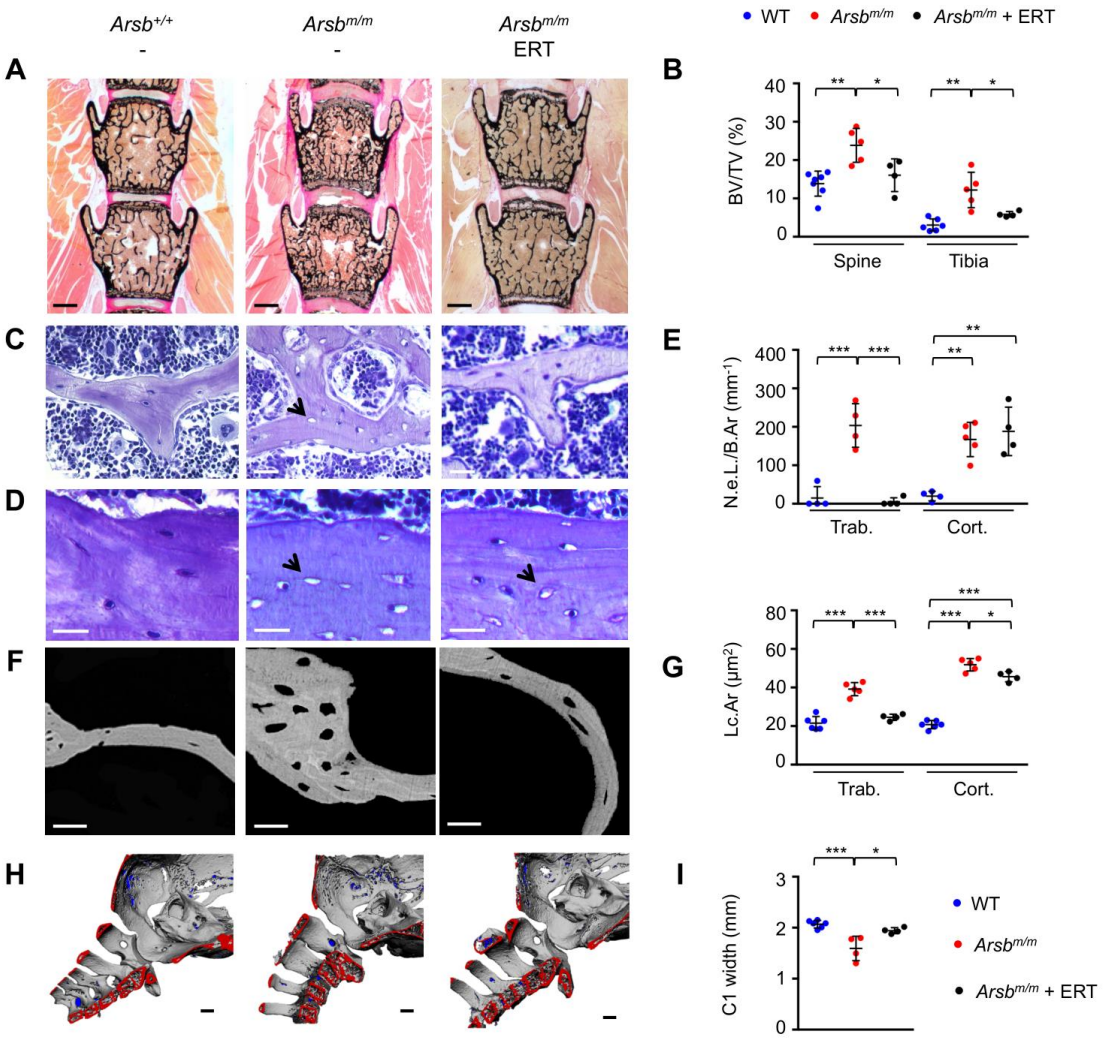

Figure 9